Electrochimica Acta 242 (2017) 400–407

Contents lists available at ScienceDirect

Electrochimica Acta

journal homepage: www.elsevier.com/locate/electacta

Evaluating the Potential Benefits of Metal Ion Doping in SnO_2 Negative Electrodes for Lithium Ion Batteries☆

Mechthild Lübke[a,b], Ding Ning[b], Ceilidh F. Armer[b,c], Dougal Howard[a], Dan J.L. Brett[d], Zhaolin Liu[b], Jawwad A. Darr[a,*]

[a] Department of Chemistry, University College London, 20 Gordon Street, London, WC1H 0AJ, UK
[b] Institute of Materials Research and Engineering (IMRE), A*STAR (Agency for Science, Technology and Research), 2 Fusionopolis Way, Innovis #08-03, Singapore 138634, Republic of Singapore
[c] College of Engineering and Computer Science, Australian National University, Canberra, ACT 0200, Australia
[d] Electrochemical Innovation Lab, Department of Chemical Engineering, University College London, Torrington Place, London, WC1E 7JE, UK

ARTICLE INFO

Article history:
Received 13 March 2017
Received in revised form 4 May 2017
Accepted 6 May 2017
Available online 8 May 2017

Keywords:
Continuous Hydrothermal Flow Synthesis
Tin dioxide
Lithium ion battery
Anode
Nano

ABSTRACT

Nine different transition metal doped (<10 at%) tin dioxides and undoped SnO_2 nanopowders with similar specific surface areas were made using a continuous hydrothermal process and then investigated as potential negative electrode materials for lithium ion batteries. The as-prepared nanopowders were characterized *via* a range of analytical techniques including powder X-ray diffraction, X-ray photoelectron spectroscopy, X-ray fluorescence spectrometry, transmission electron microscopy, thermogravimetric analysis and Brunauer-Emmett-Teller surface area measurements. Doped SnO_2 materials were grouped into two classes according to the potential redox activity of the dopant (those presumed to be redox inactive: Nb, Ti, Zr; and those presumed to be redox active: Fe, Co, Cu, Zn, Mn, Ni). The role of the transition metal ion dopant on the cycling performance (overall capacity and voltage hysteresis), was elucidated for the first cycle *via* cyclic voltammetry measurements in half cells versus lithium metal. In particular, the authors were able to evaluate whether the initial Coulombic efficiency and the delithiation potential (*vs.* Li/Li^+) of the doped samples, would be likely to offer any increased energy density (compared to undoped SnO_2) for lithium ion batteries.

1. Introduction

High energy lithium ion batteries are a key technology with the potential to meet future requirements for energy storage in hybrid electric vehicles and other portable electronic devices [1,2]. High energy can be achieved with a high cell voltage (*via* a low operating voltage negative electrode and a high operating voltage positive electrode) and high specific capacities [3]. Conversion and alloying negative electrode materials have been shown to have very high theoretical capacities, *e.g.* Fe_2O_3 = 1007 mAh g^{-1}, Si = 3579 mAh g^{-1}, Sn = 993 mAh g^{-1}, and SnO_2 = 782 mAh g^{-1} [1,4]. To date, alloying materials are favored compared to the conversion materials, due to the lower operating potential (*vs.* Li/Li^+) and far lower voltage hysteresis of the former [4]. A voltage hysteresis can be understood as a massive shift of the electrochemical potential activity from low potentials during lithiation, towards high potentials during delithiation for the negative electrode side. SnO_2 has attracted interest as a negative electrode in lithium ion batteries because it is relatively inexpensive, readily synthesized, non-toxic and shows high capacities [5–16]. The relevant electrochemical processes that occur during cycling are described in Equations 1-3:

$$x\,Li^+ + \text{electrolyte} + xe^- \rightarrow \text{SEI}\ (x\text{Li}) \quad (1)$$

$$SnO_2 + 4\,Li^+ + 4e^- \rightarrow Sn + 2\,Li_2O \quad (2)$$

$$Sn + x\,Li^+ + xe^- \leftrightarrow Li_xSn\ (0 \le x \le 4.4) \quad (3)$$

Eq. (1) corresponds to the initial solid electrolyte interphase (SEI) formation during the first and following few cycles. The conversion of SnO_2 towards metallic Sn during initial lithiation, causes extreme structural and volume changes (Eq. (2)). During further lithiation, up to 4.4 mol of lithium ions are stored in

☆ Research webpages http://www.ucl.me.uk.
* Corresponding author at: Christopher Ingold Laboratories, Department of Chemistry, University College London, 20 Gordon Street, London, WC1H 0AJ, UK.
E-mail address: j.a.darr@ucl.ac.uk (J.A. Darr).

http://dx.doi.org/10.1016/j.electacta.2017.05.029

themetallic Sn at low potentials (Eq. (3)) and this reaction is considered fully reversible. There has been considerable disagreement regarding the reversibility of the conversion process shown in Equation 2; some researchers suggest this reaction is irreversible [17–19], whilst other researchers claim it is reversible [20–22]. The origin of this disagreement can be found in the additional delithiation capacity for high surface area SnO_2 materials at higher potentials (in the range *ca.* 1.2 to 2.0 V *vs.* Li/Li^+). In an attempt to show the reversible formation of Sn^{4+}, ex-situ X-ray photoelectron spectroscopy (XPS) measurements [21,23] and ex-situ high resolution-transmission electron microscopy (HR-TEM) studies [23,24] were used after the first delithiation step at *ca.* 3.0 V *vs.* Li/Li^+. Conversely, Lee et al. suggested that the origin of this increased capacity could be mainly found in the electrochemical activity of $LiOH/LiH/LiO_2$ [25]; such species were also believe to be responsible for the additional storage capacities observed for RuO_2 (generated due to the presence of H_2O, which leads to electrochemically active LiOH in the sample) [26]. Therefore, convincing evidence for a reversible conversion reaction is still missing to date, thus, we will not discuss this further herein.

Recently, several reports have claimed that the electrochemical performance of SnO_2 could be improved by introducing transition metal dopants into the host lattice or by addition of secondary metal oxide phases. Examples of such elements include Fe [5,27–29], Cu [30], Mn [29], Co [21,29,31,32], Co-Ni [12,33], Zn [34–36], Ti [37] and Ni [38,39]. More details can be found in a comprehensive review by Bresser et al. [40]. Unfortunately, only a few of the aforementioned studies reported the specific surface areas of the doped/composite SnO_2 and the pristine SnO_2 materials. Indeed, in some cases, the surface area of the pristine SnO_2 was more than three times lower than the corresponding doped SnO_2 [5,21]. In 2000, Li et al. highlighted the importance of using nano-sizing to improve the electrochemical properties of SnO_2 [41]. This was in agreement with others, who demonstrated drastic differences in the electrochemical performance with different particle sizes (essentially higher delithiation capacities with smaller particle sizes) [42,43]. Thus, in the evaluation of both pristine and doped SnO_2 materials, synthesis methods that can facilitate materials with both high and similar surface areas are highly desirable, because this may allow a better deconvolution of the effects of the dopants on the electrochemical properties (*e.g.* specific capacity and Coulombic efficiency).

Herein, the authors employed a continuous hydrothermal flow synthesis (CHFS) method to produce undoped and doped SnO_2 materials with similar (high) surface areas, crystallinity and dopant contents at a 10 g h^{-1} production rate. The precursor concentrations used herein were with the dopant metal at a value of 10 at% (with respect to Sn). The CHFS process is described in more detail in the experimental section and supplementary information; the process has previously been used for the production of battery materials with high surface areas and narrow particle size distributions [44]. There are many negative electrode materials for lithium ion batteries that have been made *via* CHFS type processes, including anatase TiO_2 (undoped and doped with Sn or Nb) [45,46], Fe_3O_4 [47], $Li_4Ti_5O_{12}$ [48], semi-crystalline Nb_2O_5 [49], VO_2 [50], and layered titanates [51]. Nano-sized SnO_2 materials have been made previously via a continuous hydrothermal route, but have not been evaluated for lithium ion battery applications to date [52–54].

The as–prepared nano-sized doped materials were investigated using a range of analytical methods as well as being tested electrochemically as potential negative electrodes for lithium ion batteries. The transition metal dopants were grouped into two classes, namely (i) redox inactive and (ii) possible redox active dopants. Redoxinactive dopants included Nb, Ti and Zr. Redox active dopants included Fe, Co, Cu, Zn, Mn and Ni, which were classified because of the known ability of their corresponding metal oxides to undergo conversion (alloying) reactions with lithium ions [55,56]. The electrochemical performance of the as-prepared nanomaterials, was evaluated *via* potentiodynamic methods in order to assess the potentials versus lithium metal.

2. Experimental

2.1. Materials

All chemicals were used without further purification. Potassium stannate trihydrate (99.9%), titanium oxysulfate (≥29% Ti as TiO_2), ammonium niobate oxalate hydrate (99.99%) and zinc nitrate hexahydrate (98%) were purchased from Sigma-Aldrich (Dorset, UK). Cobalt nitrate hexahydrate (99%), iron (III) citrate nonahydrate (98%), copper nitrate trihydrate (99%) and zirconyl nitrate hydrate (99.5%) were purchased from Fisher Scientific, (Leicestershire, UK). Manganese nitrate tetrahydrate (98%) and nickel nitrate hexahydrate (98%) were purchased from Alfa Aesar (Lancashire, UK). For the synthesis, 0.1 M of Sn salt was used for the production of undoped SnO_2 and 0.09 M of Sn salt mixed together with 0.01 M of the respective transition metal ion salt in solution, was used for the production of doped SnO_2.

2.2. Synthesis

The nanoparticles were synthesized using a laboratory scale CHFS reactor incorporating a patented confined jet mixer (CJM), the basic design of which, can be found in the literature [57,58], see also supplementary Fig. S1. The CJM is essentially an efficient co-current mixing device made from off-the-shelf Swagelok™ fittings that efficiently allows the ambient temperature metal salt solutions to mix with the supercritical water feed to form nanoparticles "in flow" and without blockages. In the lab-scale CHFS process used herein [44], three identical diaphragm pumps (Primeroyal K, Milton Roy, Pont-Saint-Pierre, France) were used to supply three pressurized (24.1 MPa) feeds. Pump 1 supplied a feed of DI water at a flow rate of 80 mL min^{-1}, which was then heated to 450 °C in flow using a 7 kW electrical water heater. Pump 2 supplied the metal salt precursors at a flow rate of 40 mL min^{-1} and pump 3 supplied DI water at a flow rate of 40 mL min^{-1}. The feeds from pumps 2 and 3 were combined at room temperature in a dead volume tee-piece before this mixture was then brought into contact with the flow of supercritical water (co-currently) in the CJM to give a calculated mixing temperature of *ca.* 335 °C (residence time *ca.* 5 s). Upon mixing of the hot and ambient temperature feeds in flow, the metal salts rapidly reacted to give the corresponding metal oxide nanoparticles that were then cooled to *ca.* 40 °C in flow over several minutes via a heat exchanger. At the end of the CHFS process, each of the cooled particle-laden aqueous flows passed through a back-pressure regulator (BPR) and was collected in a beaker. The resulting slurry was cleaned by allowing it to settle, before dialyzing the solids with DI water (<10 MΩ) and then freeze-drying (Virtis Genesis 35XL) by cooling to −60 °C followed by slow heating under a vacuum of < 13.3 Pa over 24 h. The freeze-dried powders were used for further analyses.

2.3. Materials Characterization

Powder X-ray diffraction (PXRD) patterns of all samples were obtained on a STOE diffractometer using Mo-Kα radiation (λ = 0.70926 Å) over the 2θ range 2 to 40° with a step size of 0.5° and step time of 20 s. X-ray photoelectron spectroscopy (XPS) measurements were collected using a Thermo Scientific K-alpha

spectrometer using Al-Kα radiation and a 128-channel position sensitive detector. The XPS data were processed using CasaXPS™ software (version 2.3.16) and the binding energy scales were calibrated using the adventitious C 1s peak at 285.0 eV. Elemental composition of the samples was determined with an X-ray fluorescence spectrometer (XRF, Rh target, Bruker M4 Tornado). For recording XRF spectra, pellets of the powders were pressed under identical conditions (*ca.* 300 mg, 2 tons of force, 30 s). Lattice structural information and particle morphology were examined *via* transmission electron microscopy (TEM) with a JEOL 2100 TEM. Brunauer-Emmett-Teller (BET) surface area measurements were carried out using N_2 in a Micrometrics ASAP 2020 Automatic High-Resolution Micropore Physisorption Analyzer. The samples were degassed at 120 °C (5 h) under vacuum before measurements. Thermogravimetric analysis (TGA) was performed using a TGA Q500 instrument (TA instruments) under nitrogen with a flow rate of 40 mL min^{-1}. The test started from room temperature to 300 °C with a heating rate of 20 °C min^{-1}.

2.4. Electrochemical Characterization

The freeze-dried samples were used as the active materials in electrodes without any further post-synthesis heat treatments. The slurry for the electrode was prepared with a content of 80 wt% active materials, 10 wt% conductive agent (carbon black, Super P™, Alfa Aesar, Heysham, UK) and 10 wt% polyvinylidene fluoride, (PVDF, Kynar 761). Electrodes of undoped SnO_2 were initially prepared with a ratio of 50:40:10 and carbon black electrodes were also fabricated with a ratio of 90:10. PVDF was dissolved in *N*-methyl-2-pyrrolidone (NMP, Sigma-Aldrich, St. Louis, USA) for at least 1 h at room temperature before adding the active material and conductive agent. The mixtures were combined in a high shear mixer (model THINKY ARE-310, Thinky, CA, USA) using three cycles of mixing of 2 min duration at 2000 rpm (each cycle was followed by a defoaming step of 10 s at 2200 rpm). The doctor bladed electrodes were dried in an oven at 70 °C for 1 hour, pressed with 800 Kg of force and then left overnight at room temperature. Electrodes with a diameter of 15.0 mm were punched out, dried 12 hours at 70 °C and then overnight under vacuum. The electrodes had an active material mass loading of 1.5 ± 0.5 mg cm^{-2}.

Electrochemical experiments were performed using two-electrode CR2032-type coin cells, which were assembled in an argon-filled glovebox (MB150B-G, MBraun, Garching, Germany) with O_2 and H_2O limited to <1 ppm. The counter electrode was lithium metal foil. The separator (glass microfiber filters, Whatman, Buckinghamshire, UK) was saturated with 120 μL of 1 M $LiPF_6$ in ethylene carbonate/dimethyl carbonate (1:1 v/v, Merck Selectipur LP40, Darmstadt, Germany). The electrochemical performance was investigated by cyclic voltammetry (CV) in the range 0.05 to 3.0 V *vs.* Li/Li^+ with a scan rate of 0.1 mV s^{-1} using a galvanostat/potentiostat (PGSTAT302, AUTOLAB, Metrohm, Utrecht, Netherlands).

3. Results and Discussion

All materials were obtained as powders with different colours according to the dopant used (see Fig. 1a and Table 1). Powder XRD data for the samples revealed tetragonal SnO_2 (space group P42/mnm, ICSD 9163) as the main phase with no impurity peaks (Fig. 1b and d). Magnification of the data at lower two theta angles suggested that the materials were similarly crystalline (Fig. 1c and 1e). Scherrer crystallite size estimates using the (110) peak, suggested a crystallite size of *ca.* 6.8 nm for undoped SnO_2, 6.1 nm for $Sn_{0.9}Fe_{0.1}O_2$ and 6.3 nm for $Sn_{0.9}Co_{0.1}O_2$ (see TEM analyses later for actual crystallite sizes). XRF measurements suggested that the dopant concentrations were all in the range 6 to 10 at% (Table 1). Therefore, transition metal doping had been achieved as anticipated with no phase separation.

It is known that nanomaterials are often hygroscopic and that the presence of such water can result in the formation of LiOH that can affect the electrochemical performance of negative electrode materials such as SnO_2 (see introduction references [25,26]). Therefore, TGA measurements were undertaken on all nanomaterials (see supplementary Fig. S2) to assess water contents. A weight loss of *ca.* 3 wt% due to weakly associated water, was observed for all the nanomaterials in the temperature range 25 to 120 °C [59] (with no more than 4 wt% loss overall up to a temperature of 300 °C). Considering that the electrodes made herein were heated and dried overnight under vacuum (*via* the glovebox), it is safe to suggest there should have been <1 wt% water in the active materials.

The high-resolution XPS spectrum of the Sn 3d region (supplementary Fig. S3), revealed two peaks corresponding to the binding energies for Sn 3d5/2 at 486.1 eV and Sn 3d3/2 at 494.5 eV, which were assigned to Sn^{4+} and were observed in a similar range for all materials. The XPS spectra for all dopants are presented in supplementary Fig. S4 and discussed further in the supplementary information. The oxidation state of the metal ions in the precursors did not change (except partly for Fe and Mn) during the synthesis and therefore, all doped transition metals remained (mainly) in the same oxidation state as their respective precursor solutions (Table 1).

The morphology, size and crystallinity were examined by TEM (Fig. 2). The particles had a rod-like morphology (and spherical), appeared to be slightly aggregated and were monocrystalline. The inset in Fig. 2a and 2b displayed an interlayer spacing of 0.34 nm (110) for both undoped SnO_2 and $Sn_{0.91}Co_{0.09}O_2$. The undoped SnO_2 appeared to show more rod-like particles compared to Co-doped SnO_2, which showed more spherical particles (Fig. 2c). The average measured crystallite sizes were in a similar range for both undoped SnO_2 (mean particle length 10.6 nm, mean particle width 5.0 nm; >160 particles sampled) and $Sn_{0.91}Co_{0.09}O_2$ (mean particle length 8.7 nm, mean particle width 5.5 nm; >160 particles sampled), which is in line with the similar surface areas of *ca.* 95.1 and 99.6 $m^2 g^{-1}$ for undoped and Co-doped SnO_2, respectively. The BET surface areas of all nanoparticle samples were in the range 85.4 to 123.3 $m^2 g^{-1}$, see Table 1.

Overall, the CHFS process facilitated the synthesis of various as-prepared doped SnO_2 materials with similar surface areas, crystallinity and dopant concentration. The oxidation state of the dopant was controlled by the choice of precursor in solution. Thus, for electrochemical investigations versus lithium metal in a half-cell configuration, the effects of the dopant transition metal on the electrochemical properties could be compared without considering any significant differences in the surface area, crystallinity or water content.

In order to compensate for extreme volume expansions that occur during cycling in SnO_2 negative electrodes, high conductive carbon loadings are often used in the literature (typically equating to <63 wt% SnO_2 [5–16,60–62]) to allow cells to cycle well without catastrophic capacity fading. The carbon in such cells can be introduced *via* carbon coating, addition of graphene, carbon black etc. Therefore, the authors first measured the specific capacity for undoped SnO_2 electrodes with only 50 wt% active material in order to ascertain the baseline electrode performance. In Fig. 3a, the CV is plotted for undoped SnO_2 and the contributions of the carbon black were calculated based on similar measurements with pure carbon black electrodes (see red area Fig. 3a). Pure SnO_2 underwent two types of lithiation processes, namely the initial conversion to Sn metal and Li_2O at *ca.* 0.96 V *vs.* Li/Li^+ (Eq. (2)) and the alloying reaction of the Sn metal with lithium ions towards Li_xSn ($0 \leq x \leq 4.4$) at *ca.* 0.22 V *vs.* Li/Li^+ (Eq. (3)). There was an additional

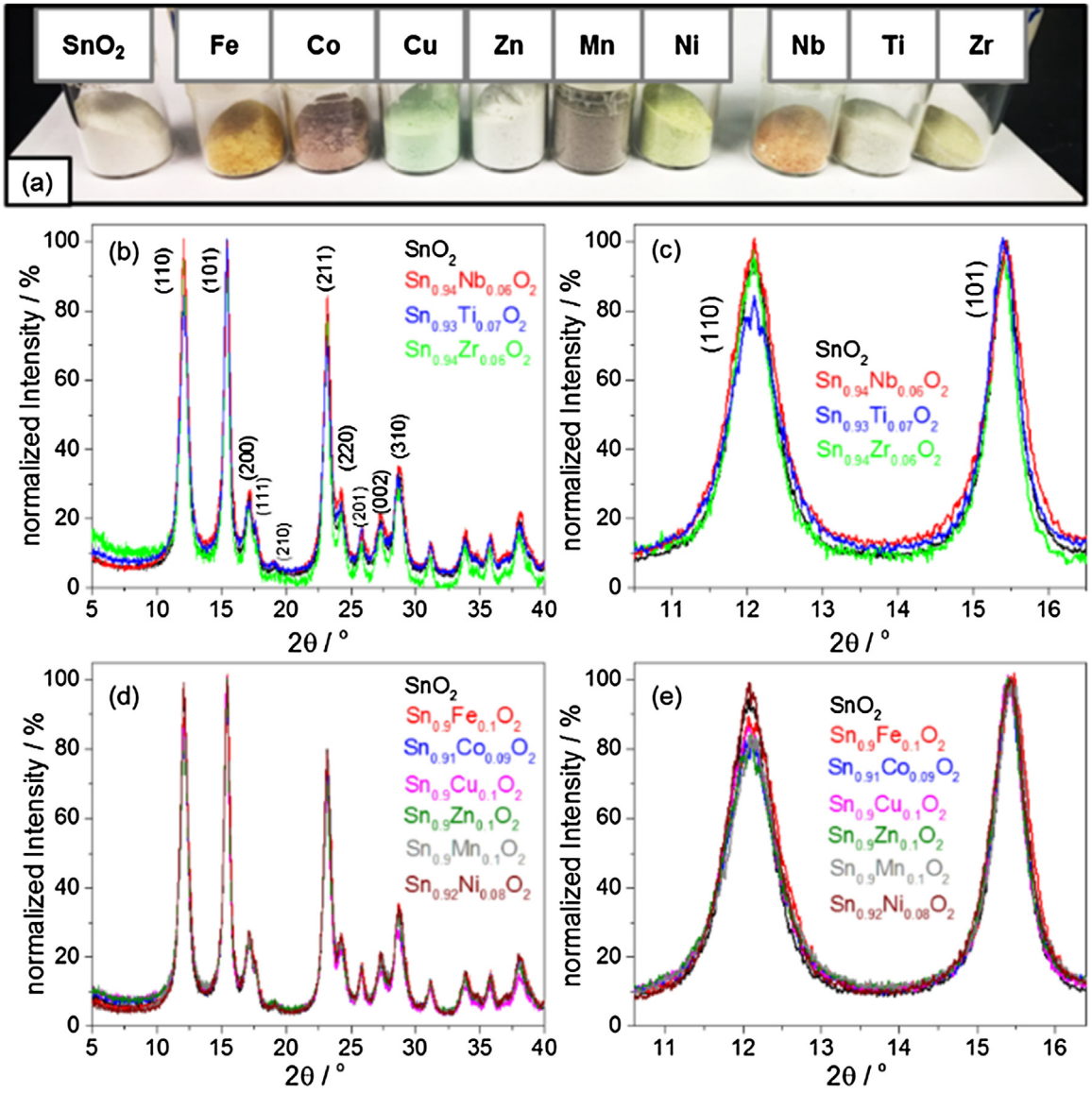

Fig. 1. (a) Photo showing the colour of the doped SnO_2 nanoparticles alongside undoped SnO_2. PXRD patterns [normalized to the (101) peak intensity] for potential redox inactive dopants in SnO_2 and undoped SnO_2 in the 2θ range (b) 5.0 to 40.0° and (c) 10.5 to 16.5°. PXRD patterns [normalized to the (101) peak intensity] for potential redox active dopants in SnO_2 and undoped SnO_2 in the 2θ range (d) 5.0 to 40.0° and (e) 10.5 to 16.5°.

Table 1
Characterization of the synthesized materials. The colour is based on the photograph in Fig. 1a, the dopant concentration was obtained *via* XRF, the oxidation state of the dopant was identified with XPS measurements and the specific surface area was obtained *via* BET surface area measurements. All dopants were split into two groups, namely possibly redox active (conversion reaction ability) and inactive dopants. The calculated capacities are based on analysis of the CVs for the first cycle.

Sample	Colour	Dopant conc. /at%	Oxidation state dopant	Surface area/ $m^2 g^{-1}$	Expected dopant reactivity	Lithiation capacity/ mAh g^{-1}	Delithiation capacity/ mAh g^{-1}	Coulombic efficiency/%
SnO_2	white	0	–	95.1	–	1299.8	812.2	62.5
$Sn_{0.94}Nb_{0.06}O_2$	light yellow	5.8	5+	112.5	redox inactive	960.4	633.2	65.9
$Sn_{0.93}Ti_{0.07}O_2$	white	7.3	4+	110.8		1061.2	600.8	56.6
$Sn_{0.94}Zr_{0.06}O_2$	light grey	6.1	4+	98.0		1066.0	628.1	58.9
$Sn_{0.9}Fe_{0.1}O_2$	yellow	9.9	2+/3+	123.1	redox active	1283.2	753.9	58.8
$Sn_{0.91}Co_{0.09}O_2$	brown	9.0	2+	99.6		1199.7	952.9	79.4
$Sn_{0.9}Cu_{0.1}O_2$	light green	10.4	2+	102.0		1314.7	838.9	63.8
$Sn_{0.9}Zn_{0.1}O_2$	white	9.8	2+	98.4		1256.8	800.7	63.7
$Sn_{0.9}Mn_{0.1}O_2$	dark brown	9.6	2+/3+	85.4		1323.8	845.8	63.9
$Sn_{0.92}Ni_{0.08}O_2$	light green	8.2	2+	99.8		1164.7	802.5	68.9

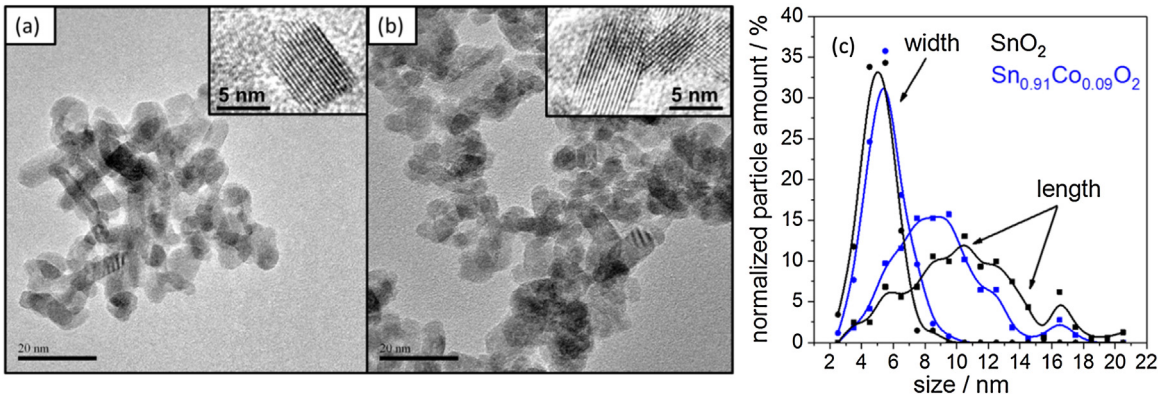

Fig. 2. TEM images of (a) undoped SnO_2 (bar = 20 nm) and (b) $Sn_{0.91}Co_{0.09}O_2$ (bar = 20 nm). HRTEM inset is shown on the top right of each figure (bar = 5 nm). (c) Normalized particle amount plotted for the size parameters width and length (>160 particles sampled).

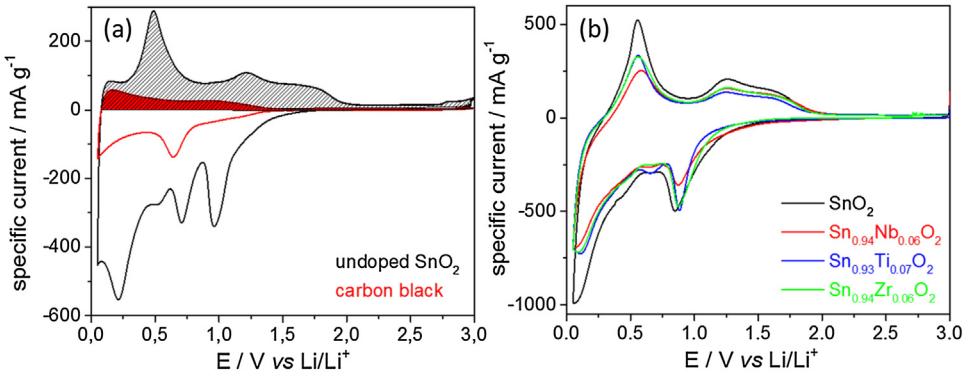

Fig. 3. (a) CVs of the first cycle at a scan rate of 0.1 mV s^{-1} for undoped SnO_2 versus carbon black. The electrode loading wt% ratio was 50:40:10 for SnO_2:Carbon:PVDF, respectively. (b) Cyclic voltammograms at a scan rate of 0.1 mV s^{-1} for all expected redox inactive dopants in comparison to undoped SnO_2. The electrode loading wt% ratio was 80:10:10 for SnO_2:Carbon:PVDF, respectively.

peak at *ca.* 0.70 V *vs.* Li/Li^+, which was due to SEI formation (Eq. (3)) on the carbon additive, see comparison with carbon black electrode and also the results from Fransson et al. [63]. During delithiation, the lithiated Sn compound dealloyed at *ca.* 0.50 V *vs.* Li/Li^+ and also showed additional redox activity at higher potentials (>1.0 V *vs.* Li/Li^+). As shown, the additional charge/discharge activity of the carbon additive was not negligible, since *ca.* 87 mAh g^{-1} could be stored and released during delithiation. This meant that from the overall specific capacity of 511 mAh g^{-1}, *ca.* 17 % of the delithiation capacity could have been due to the contribution from the carbon, see also [63]. If only the delithiation capacity was calculated (based on undoped SnO_2 with no contributions from the carbon assumed), the specific capacity would have been 986 mAh g^{-1}. Clearly, the electrochemical lithiation/delithiation in a carbon/active material composite electrodes is still not fully understood and an exact determination of the individual capacity contributions of each material in the composite is not possible. With this in mind, only 10 wt% carbon content electrodes were used for further electrochemical testing as to minimize the additional electrochemical contributions from it.

The CVs for samples $Sn_{0.94}Nb_{0.06}O_2$, $Sn_{0.93}Ti_{0.07}O_2$ and $Sn_{0.94}Zr_{0.06}O_2$ (assumed redox inactive dopants) versus SnO_2 are presented in Fig. 3b. The lithiation and delithation activity was lower at all potentials for the doped materials compared to the undoped SnO_2, suggesting that the dopant did not impart any benefit on improving the capacity performance. Similar to these results, no capacity improvement at low currents has been previously reported in the literature for Ti-doped SnO_2 versus undoped SnO_2 with similar surface areas (26 and 21 $m^2 g^{-1}$, respectively [37]).

The CV results of all possible redox-active dopants are shown in Fig. 4a. These dopants might have the potential to (partially) undergo a conversion reaction themselves. It is known that the energy density is related to the full cell voltage multiplied by the charge for an ideal battery. Therefore, the wider the potential window, the more energy that can be stored. With this in mind, the authors sought to identify the location of the potential peaks for charge and discharge in the doped materials and make qualitative assessments on the likely energy density that would result (particularly if they were to be made into full cells in the future).

In Fig. 4b, the lithiation peaks are presented *via* a specific current versus potential plot and the corresponding specific lithiation capacities are given in Table 1. Pure SnO_2 underwent two lithiation steps, namely the initial conversion towards Sn metal and Li_2O at *ca.* 0.85 V *vs.* Li/Li^+ (Equation 2) and the alloying reaction of the Sn metal with lithium ions towards Li_xSn ($0 \leq x \leq 4.4$) at *ca.* 0.1 V *vs.* Li/Li^+ (Equation 3). These potentials for the conversion and alloying reactions were lower than those shown in Fig. 3a. This might be due to increased electrode resistance due to the relatively low carbon content in the majority of the electrodes. All samples showed two lithiation peaks, although the alloying peak was less strong for the doped samples compared to the undoped counterpart, which could be attributed to the lower concentration of Sn atoms in the materials. The conversion peak was higher for the majority of the redox-active dopants (except for Ni and Fe), which might have corresponded to

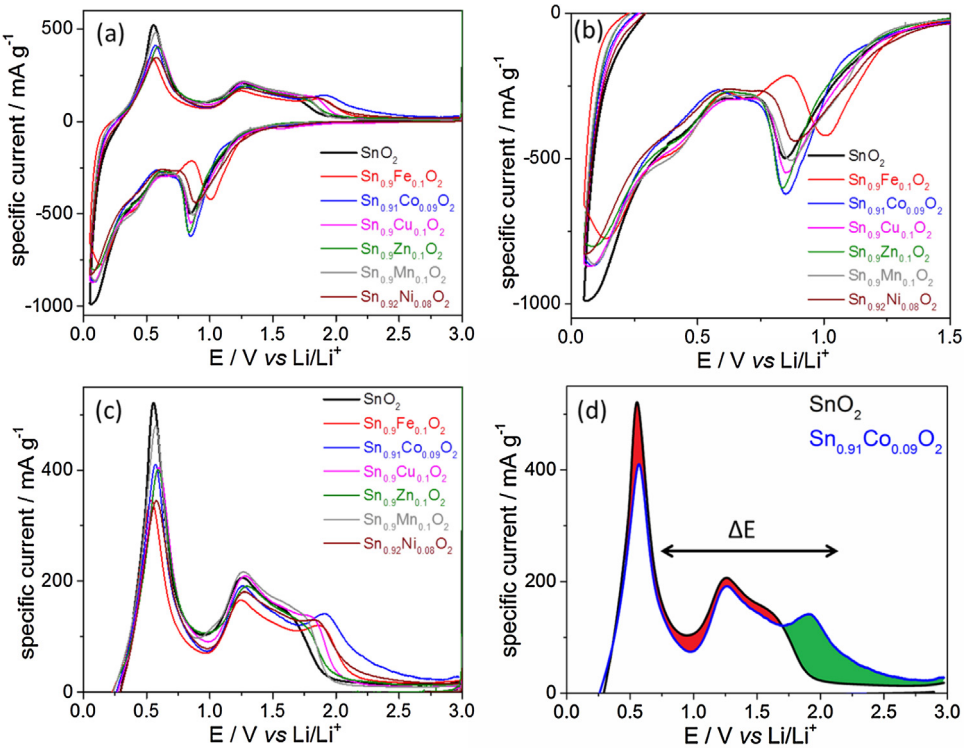

Fig. 4. CVs of the first cycle at a scan rate of 0.1 mV s^{-1}. (a) Illustration of all CVs for possible redox active dopants, (b) focus on the lithiation performance and (c) focus on the delithiation performance showing that for all materials, there is a capacity loss at lower potentials and a capacity win at higher potentials. A schematic plot is presented in (d) with the capacity loss shown in the red area and gain in the green area. The electrode loading wt% ratio was 80:10:10 for SnO_2:Carbon:PVDF, respectively. (For interpretation of the references to colour in this figure legend, the reader is referred to the web version of this article.)

the initial reduction of CoO [55,64], CuO [65], ZnO [66] and Mn_2O_3 [67]. Moreover, $Sn_{0.9}Mn_{0.1}O_2$ showed a shoulder around 0.4 V *vs.* Li/Li^+, which might be related to the Mn oxide in the sample [67]. NiO may already be active at *ca.* 1.0 V *vs.* Li/Li^+ [68], which may be so with the results herein, since the first lithiation peak was broader compared to the undoped SnO_2. Sample $Sn_{0.9}Fe_{0.1}O_2$ showed a broader lithiation peak at *ca.* 1.0 V and a second smaller one at *ca.* 0.6 V *vs.* Li/Li^+. Overall, these results may be an indication that all "conversion-type" dopants remained (partly) electrochemically active during cycling, which would be in agreement with the author's previous report (where the Sn was the dopant and it could be activated in nano-sized TiO_2 [45]). The first lithiation capacities were all in the range of *ca.* 1165 to 1324 mAh g^{-1}. As there were many potential contributions in addition to the SnO_2 activity for these capacities (*e.g.* SEI formation, possible electrochemical activity of the dopant), the origin of all lithiation contributions is not further discussed in detail hereafter.

In Fig. 4c, the delithiation performance was plotted for all SnO_2 samples doped with possible redox active dopants. The undoped SnO_2 showed the highest measured current for the dealloying peak at *ca.* 0.55 V *vs.* Li/Li^+, which can be again explained with the highest concentration of Sn atoms of any sample. Overall, there was no observed capacity win for any sample during delithiation until 1.5 V *vs.* Li/Li^+. However, there was a capacity win for all (potential) redox active dopants at potentials higher than 1.7 V *vs.* Li/Li^+, which might be explained by the additional delithiation reactions from the conversion of the doped transition metal. CuO based electrode materials might have been expected to show additional delithiation activity at 2.5 V *vs.* Li/Li^+ [65], which was not observed herein and was also not observed for other Cu/Sn oxide composite negative electrode materials [30,69,70]. Overall, the samples containing either Fe, Co or Ni, clearly showed the largest capacity wins at higher potentials.

In Fig. 4d, the delithiation performance is summarized in a scheme with the data from sample $Sn_{0.91}Co_{0.09}O_2$. All SnO_2 based materials containing dopants that were presumably redox active, showed a capacity loss relative to undoped SnO_2 at lower potentials (<*ca.* 1.2 V *vs.* Li/Li^+), but a capacity win at higher potentials (>*ca.* 1.7 V *vs.* Li/Li^+). Similar results were obtained recently for molybdenum-tin oxide composites, which showed a higher capacity compared to undoped SnO_2, but additional delithiation processes occurred at higher potentials [71]. Herein, $Sn_{0.9}Cu_{0.1}O_2$ and $Sn_{0.9}Mn_{0.1}O_2$ showed slightly higher delithiation capacities compared to undoped SnO_2. Overall, taking into account the samples are all of similar surface areas and crystallinity, sample $Sn_{0.91}Co_{0.09}O_2$ outperformed the undoped SnO_2 and all other samples in terms of Coulombic efficiency and specific capacity (Table 1). This is unsurprising given the current interest in Co-Sn oxides in the literature [21,31,32,72–75] and would explain the current commercial and academic interest in composite C-Sn-Co negative electrodes, *e.g.* in Nexelion batteries from Sony (where the wt% ratio of graphite:Sn:Co was 50:25:25) [76].

The question remains as to whether such mixed conversion and alloying materials would be expected to offer gains in terms of energy density if they were evaluated in full cells. Meister et al. recently investigated various types of lithium ion battery full cells and showed that for all investigated negative active materials (Si/C *vs.* graphite *vs.* soft carbon *vs.* $ZnFe_2O_4$), energy inefficiency was mainly caused by a voltage hysteresis between the charge and discharge curve [77]. As stated before, the energy density of the full cell might be simply understood as the mathematical product of full cell voltage and specific capacity. This, in turn, means that a slight capacity win for a composite material (herein especially $Sn_{0.9}Cu_{0.1}O_2$) might not give a larger energy density compared to undoped SnO_2, since a high cell voltage is sacrificed through the voltage hysteresis at the same time. Overall, it was observed that if

the material's properties of doped SnO_2 were similar to the undoped one, the benefits (towards high energy full cells) of doping might not be as evident as proposed by many reports in the literature. The dopant might have an impact on the cycle stability and rate capability. However, no effective buffer was used herein limiting credible investigations. For such a study, carbon/SnO_2 composites might be used, where the undoped and doped materials show again similar materials properties.

4. Conclusions

In this study, various doped SnO_2 nanomaterials were made in a single step using a continuous hydrothermal flow synthesis route. The as-prepared materials could be directly used (and compared) as potential negative electrode materials for lithium ion batteries because they were synthesized with similar dopant concentrations, surface area, crystallinity and water content. Investigation of the specific capacities as well as a the location of the peak potentials for the redox events during cycling, suggested that doping may not necessarily be beneficial for increasing energy density if the electrodes were to be used in full cells in the future. Only the sample with 9 wt% Co was observed to stand out due to a delithiation capacity increase from 812 mAh g^{-1} for undoped SnO_2 to 953 mAh g^{-1} with increased Coulombic efficiency (79.4 % for the Co-doped sample versus 62.5 % for undoped SnO_2).

Acknowledgements

The EPSRC are thanked for funding the Centre for Doctoral Training in Molecular Modelling & Materials Science (EPSRC reference EP/L015862/1) which has supported M.L. and funding the ELEVATE project [ELEctrochemical Vehicle Advanced Technology, EPSRC reference EP/M009394/1] (J.A.D.). A Star (Singapore) and UCL are thanked for supporting a studentship for M.L. Ms Hui Ru TAN is thanked for the TEM images.

Appendix A. Supplementary data

Supplementary data associated with this article can be found, in the online version, at 10.1016/j.electacta.2017.05.029.

References

[1] M.R. Palacin, Recent advances in rechargeable battery materials: A chemist's perspective, Chemical Society Reviews 38 (2009) 2565–2575.
[2] B. Dunn, H. Kamath, J.-M. Tarascon, Electrical energy storage for the grid: A battery of choices, Science 334 (2011) 928–935.
[3] M. Winter, R.J. Brodd, What are batteries, fuel cells, and supercapacitors? Chemical Reviews 104 (2004) 4245–4270.
[4] L. Croguennec, M.R. Palacin, Recent achievements on inorganic electrode materials for lithium-ion batteries, Journal of the American Chemical Society 137 (2015) 3140–3156.
[5] F. Mueller, D. Bresser, V.S.K. Chakravadhanula, S. Passerini, Fe-doped SnO_2 nanoparticles as new high capacity anode material for secondary lithium-ion batteries, Journal of Power Sources 299 (2015) 398–402.
[6] G. Zhou, D.W. Wang, L. Li, N. Li, F. Li, H.M. Cheng, Nanosize SnO_2 confined in the porous shells of carbon cages for kinetically efficient and long-term lithium storage, Nanoscale 5 (2013) 1576–1582.
[7] Y. Liu, X. Yan, J.L. Lan, D. Teng, Y. Yu, X. Yang, Ti-doped SnO_x encapsulated in carbon nanofibers with enhanced lithium storage properties, Electrochimica Acta 137 (2014) 9–16.
[8] J. Liang, X.Y. Yu, H. Zhou, H.B. Wu, S. Ding, X.W.D. Lou, Bowl-like SnO_2@ carbon hollow particles as an advanced anode material for lithium-ion batteries, Angewandte Chemie International Edition 53 (2014) 12803–12807.
[9] X. Wang, X. Cao, L. Bourgeois, H. Guan, S. Chen, Y. Zhong, D.M. Tang, H. Li, T. Zhai, L. Li, N-Doped graphene-SnO_2 sandwich paper for high-performance lithium-ion batteries, Advanced Functional Materials 22 (2012) 2682–2690.
[10] M. Ara, V.R. Chitturi, S.O. Salley, K.S. Ng, Nitrogen-doped carbon-coated Sn_xO_y (x = 1 and y = 0 and 2) nanoparticles for rechargeable Li-ion batteries, Electrochimica Acta 161 (2015) 269–278.
[11] X. Zhou, L. Yu, X.W.D. Lou, Formation of uniform N-doped carbon-coated SnO_2 submicroboxes with enhanced lithium storage properties, Advanced Energy Materials 6 (2016) 1600451.
[12] X. Xu, S. Chen, C. Xiao, K. Xi, C. Guo, S. Guo, S. Ding, D. Yu, R.V. Kumar, Rational design of $NiCoO_2$@SnO_2 heterostructure attached on amorphous carbon nanotubes with improved lithium storage properties, ACS Applied Materials & Interfaces 8 (2016) 6004–6010.
[13] L. Shen, F. Liu, G. Chen, H. Zhou, Z. Le, H.B. Wu, G. Wang, Y. Lu, Encapsulation of SnO_2 nanocrystals into hierarchically porous carbon by melt infiltration for high-performance lithium storage, Journal of Materials Chemistry A 4 (2016) 18706–18710.
[14] F.M. Hassan, Z. Chen, A. Yu, Z. Chen, X. Xiao, Sn/SnO_2 embedded in mesoporous carbon nanocomposites as negative electrode for lithium ion batteries, Electrochimica Acta 87 (2013) 844–852.
[15] K. Zhao, L. Zhang, R. Xia, Y. Dong, W. Xu, C. Niu, L. He, M. Yan, L. Qu, L. Mai, SnO_2 Quantum dots@ graphene oxide as a high-rate and long-life anode material for lithium-ion batteries, Small 12 (2016) 588–594.
[16] B. Huang, X. Li, Y. Pei, S. Li, X. Cao, R.C. Massé, G. Cao, Novel carbon-encapsulated porous SnO_2 anode for lithium-ion batteries with much improved cyclic stability, Small 12 (2016) 1945–1955.
[17] J.S. Chen, Y.L. Cheah, Y.T. Chen, N. Jayaprakash, S. Madhavi, Y.H. Yang, X.W. Lou, SnO_2 nanoparticles with controlled carbon nanocoating as high-capacity anode materials for lithium-ion batteries, The Journal of Physical Chemistry C 113 (2009) 20504–20508.
[18] M.S. Park, Y.M. Kang, G.X. Wang, S.X. Dou, H.K. Liu, The effect of morphological modification on the electrochemical properties of SnO_2 nanomaterials, Advanced Functional Materials 18 (2008) 455–461.
[19] Y.D. Ko, J.G. Kang, J.G. Park, S. Lee, D.W. Kim, Self-supported SnO_2 nanowire electrodes for high-power lithium-ion batteries, Nanotechnology 20 (2009) 455701.
[20] R. Demir-Cakan, Y.S. Hu, M. Antonietti, J. Maier, M.M. Titirici, Facile one-pot synthesis of mesoporous SnO_2 microspheres via nanoparticles assembly and lithium storage properties, Chemistry of Materials 20 (2008) 1227–1229.
[21] Y. Wang, Z.X. Huang, Y. Shi, J.I. Wong, M. Ding, H.Y. Yang, Designed hybrid nanostructure with catalytic effect: beyond the theoretical capacity of SnO_2 anode material for lithium ion batteries, Scientific Reports 5 (2015) 9164.
[22] D. Mhamane, V. Aravindan, D. Taneja, A. Suryawanshi, O. Game, M. Srinivasan, S. Ogale, Graphene based nanocomposites for alloy (SnO_2), and conversion (Fe_3O_4) type efficient anodes for Li-ion battery applications, Composites Science and Technology 130 (2016) 88–95.
[23] Z. Chen, M. Zhou, Y. Cao, X. Ai, H. Yang, J. Liu, In situ generation of few-layer graphene coatings on SnO_2-SiC core-shell nanoparticles for high-performance lithium-ion storage, Advanced Energy Materials 2 (2012) 95–102.
[24] X. Guo, X. Fang, Y. Sun, L. Shen, Z. Wang, L. Chen, Lithium storage in carbon-coated SnO_2 by conversion reaction, Journal of Power Sources 226 (2013) 75–81.
[25] S.Y. Lee, K.Y. Park, W.S. Kim, S. Yoon, S.H. Hong, K. Kang, M. Kim, Unveiling origin of additional capacity of SnO_2 anode in lithium-ion batteries by realistic ex situ TEM analysis, Nano Energy 19 (2016) 234–245.
[26] Y.Y. Hu, Z. Liu, K.-W. Nam, O.J. Borkiewicz, J. Cheng, X. Hua, M.T. Dunstan, X. Yu, K.M. Wiaderek, L.S. Du, Origin of additional capacities in metal oxide lithium-ion battery electrodes, Nature Materials 12 (2013) 1130–1136.
[27] W. Xie, S. Li, S. Wang, S. Xue, Z. Liu, X. Jiang, D. He, N-doped amorphous carbon coated Fe_3O_4/SnO_2 coaxial nanofibers as a binder-free self-supported electrode for lithium ion batteries, ACS Applied Materials & Interfaces 6 (2014) 20334–20339.
[28] D.J. Ryu, H.W. Jung, S.H. Lee, D.J. Park, K.S. Ryu, The application of catalyst-recovered SnO_2 as an anode material for lithium secondary batteries, Environmental Science and Pollution Research 23 (2016) 15015–15022.
[29] R. Hu, Y. Ouyang, T. Liang, H. Wang, J. Liu, J. Chen, C. Yang, L. Yang, M. Zhu, Stabilizing the nanostructure of SnO_2 anodes by transition metals: A route to achieve high initial Coulombic efficiency and stable capacities for lithium storage, Advanced Materials 29 (2017) 1605006.
[30] B. Lu, H. Wang, R. Hu, L. Yang, J. Liu, J. Liu, M. Zhu, Enhanced cyclic performance of SnO_2-CuO-graphite nano-sheets as anode for Li-ion battery, Materials Letters 185 (2016) 9–12.
[31] N. Wan, X. Lu, Y. Wang, W. Zhang, Y. Bai, Y.S. Hu, S. Dai, Improved Li storage performance in SnO_2 nanocrystals by a synergetic doping, Scientific Reports 6 (2016) 18978.
[32] X. Zhang, X. Huang, X. Zhang, L. Xia, B. Zhong, T. Zhang, G. Wen, Flexible carbonized cotton covered by graphene/Co-doped SnO_2 as free-standing and binder-free anode material for lithium-ions batteries, Electrochimica Acta 222 (2016) 518–527.
[33] G. Gao, H.B. Wu, S. Ding, X.W.D. Lou, Preparation of carbon-coated $NiCo_2O_4$@ SnO_2 hetero-nanostructures and their reversible lithium storage properties, Small 11 (2015) 432–436.
[34] F. Belliard, P. Connor, J. Irvine, Doped tin oxides as potential lithium ion battery negative electrodes, Ionics 5 (1999) 450–454.
[35] N. Feng, L. Qiao, D. Hu, X. Sun, P. Wang, D. He, Synthesis, characterization, and lithium-storage of ZnO-SnO_2 hierarchical architectures, RSC Advances 3 (2013) 7758–7764.
[36] L. Qin, S. Liang, X. Tan, A. Pan, Zn_2SnO_4/graphene composites as anode materials for high performance lithium-ion batteries, Journal of Alloys and Compounds 692 (2017) 124–130.
[37] H. Wang, L. Xi, J. Tucek, Y. Zhan, T.F. Hung, S.V. Kershaw, R. Zboril, C.Y. Chung, A. L. Rogach, Hierarchical assembly of Ti(IV)/Sn(II) co-doped SnO_2 nanosheets

along sacrificial titanate nanowires: synthesis, characterization and electrochemical properties, Nanoscale 5 (2013) 9101–9109.
[38] Q. Zhu, P. Wu, J. Zhang, W. Zhang, Y. Zhou, Y. Tang, T. Lu, Cyanogel-derived formation of 3D Nanoporous SnO_2–M_xO_y (M = Ni, Fe, Co) hybrid networks for high-performance lithium storage, ChemSusChem 8 (2015) 131–137.
[39] V.A. Agubra, L. Zuniga, D. Flores, H. Campos, J. Villarreal, M. Alcoutlabi, A comparative study on the performance of binary SnO_2/NiO/C and Sn/C composite nanofibers as alternative anode materials for lithium ion batteries, Electrochimica Acta 224 (2017) 608–621.
[40] D. Bresser, S. Passerini, B. Scrosati, Leveraging valuable synergies by combining alloying and conversion for lithium-ion anodes, Energy & Environmental Science 9 (2016) 3348–3367.
[41] N. Li, C.R. Martin, B. Scrosati, A high-rate, high-capacity, nanostructured tin oxide electrode, Electrochemical and Solid-State Letters 3 (2000) 316–318.
[42] C. Kim, M. Noh, M. Choi, J. Cho, B. Park, Critical size of a nano SnO_2 electrode for Li-secondary battery, Chemistry of Materials 17 (2005) 3297–3301.
[43] L. Yuan, Z. Guo, K. Konstantinov, H.K. Liu, S. Dou, Nano-structured spherical porous SnO_2 anodes for lithium-ion batteries, Journal of Power Sources 159 (2006) 345–348.
[44] C.J. Denis, C.J. Tighe, R.I. Gruar, N.M. Makwana, J.A. Darr, Nucleation and growth of cobalt oxide nanoparticles in a continuous hydrothermal reactor under laminar and turbulent flow, Crystal Growth & Design 15 (2015) 4256–4265.
[45] M. Lübke, I. Johnson, N.M. Makwana, D. Brett, P. Shearing, Z. Liu, J.A. Darr, High power TiO_2 and high capacity Sn-doped TiO_2 nanomaterial anodes for lithium-ion batteries, Journal of Power Sources 294 (2015) 94–102.
[46] M. Lübke, J. Shin, P. Marchand, D. Brett, P. Shearing, Z. Liu, J.A. Darr, Highly pseudocapacitive Nb-doped TiO_2 high power anodes for lithium-ion batteries, Journal of Materials Chemistry A 3 (2015) 22908–22914.
[47] M. Lübke, N.M. Makwana, R. Gruar, C. Tighe, D. Brett, P. Shearing, Z. Liu, J.A. Darr, High capacity nanocomposite Fe_3O_4/Fe anodes for Li-ion batteries, Journal of Power Sources 291 (2015) 102–107.
[48] H. Hayashi, T. Nakamura, T. Ebina, Hydrothermal synthesis of $Li_4Ti_5O_{12}$ nanoparticles using a supercritical flow reaction system, Journal of the Ceramic Society of Japan 122 (2014) 78–82.
[49] M. Lübke, A. Sumboja, I.D. Johnson, D.J. Brett, P.R. Shearing, Z. Liu, J.A. Darr, High power nano-Nb_2O_5 negative electrodes for lithium-ion batteries, Electrochimica Acta 192 (2016) 363–369.
[50] M. Lübke, N. Ding, M.J. Powell, D.J. Brett, P.R. Shearing, Z. Liu, J.A. Darr, VO_2 nano-sheet negative electrodes for lithium-ion batteries, Electrochemistry Communications 64 (2016) 56–60.
[51] M. Lübke, P. Marchand, D.J. Brett, P. Shearing, R. Gruar, Z. Liu, J.A. Darr, High power layered titanate nano-sheets as pseudocapacitive lithium-ion battery anodes, Journal of Power Sources 305 (2016) 115–121.
[52] Z. Fang, H. Assaaoudi, H. Lin, X. Wang, I.S. Butler, J.A. Kozinski, Synthesis of nanocrystalline SnO_2 in supercritical water, Journal of Nanoparticle Research 9 (2007) 683–687.
[53] H.L. Hellstern, J. Becker, P. Hald, M. Bremholm, A. Mamakhel, B.B. Iversen, Development of a dual-stage continuous flow reactor for hydrothermal synthesis of hybrid nanoparticles, Industrial & Engineering Chemistry Research 54 (2015) 8500–8508.
[54] G.W. Chu, Q.H. Zeng, Z.G. Shen, H.K. Zou, J.F. Chen, Preparation of SnO_2 nanoparticles using a helical tube reactor via continuous hydrothermal route, Chemical Engineering Journal 253 (2014) 78–83.
[55] P. Poizot, S. Laruelle, S. Grugeon, L. Dupont, J.M. Tarascon, Nano-sized transition-metal oxides as negative-electrode materials for lithium-ion batteries, Nature 407 (2000) 496–499.
[56] J. Cabana, L. Monconduit, D. Larcher, M.R. Palacín, Beyond intercalation-based Li-ion batteries: The state of the art and challenges of electrode materials reacting through conversion reactions, Advanced Materials 22 (2010) E170–E192.
[57] J.A. Darr, M. Poliakoff, New directions in inorganic and metal-organic coordination chemistry in supercritical fluids, Chemical Reviews 99 (1999) 495–542.
[58] R.I. Gruar, C.J. Tighe, J.A. Darr, Scaling-up a confined jet reactor for the continuous hydrothermal manufacture of nanomaterials, Industrial & Engineering Chemistry Research 52 (2013) 5270–5281.
[59] J. Zhu, Z. Lu, S.T. Aruna, D. Aurbach, A. Gedanken, Sonochemical synthesis of SnO_2 nanoparticles and their preliminary study as Li insertion electrodes, Chemistry of Materials 12 (2000) 2557–2566.
[60] M.S.A. Sher Shah, J. Lee, A.R. Park, Y. Choi, W.J. Kim, J. Park, C.H. Chung, J. Kim, B. Lim, P.J. Yoo, Ultra-fine SnO_2 nanoparticles doubly embedded in amorphous carbon and reduced graphene oxide (rGO) for superior lithium storage, Electrochimica Acta 224 (2017) 201–210.
[61] Y. Li, Y. Zhao, C. Ma, Y. Zhao, Novel solvent-thermal preparation of a SnO_2 nanoparticles/expanded graphite multiscale composite with extremely enhanced electrical performances for Li-ion batteries, Electrochimica Acta 218 (2016) 191–198.
[62] L. Chen, X. Ma, M. Wang, C. Chen, X. Ge, Hierarchical porous SnO_2/reduced graphene oxide composites for high-performance lithium-ion battery anodes, Electrochimica Acta 215 (2016) 42–49.
[63] L. Fransson, T. Eriksson, K. Edström, T. Gustafsson, J.O. Thomas, Influence of carbon black and binder on Li-ion batteries, Journal of Power Sources 101 (2001) 1–9.
[64] D. Li, L.X. Ding, S. Wang, D. Cai, H. Wang, Ultrathin and highly-ordered CoO nanosheet arrays for lithium-ion batteries with high cycle stability and rate capability, Journal of Materials Chemistry A 2 (2014) 5625–5630.
[65] W. Yang, J. Wang, W. Ma, C. Dong, G. Cheng, Z. Zhang, Free-standing CuO nanoflake arrays coated Cu foam for advanced lithium ion battery anodes, Journal of Power Sources 333 (2016) 88–98.
[66] G.L. Xu, Y. Li, T. Ma, Y. Ren, H.H. Wang, L. Wang, J. Wen, D. Miller, K. Amine, Z. Chen, PEDOT-PSS coated ZnO/C hierarchical porous nanorods as ultralong-life anode material for lithium ion batteries, Nano Energy 18 (2015) 253–264.
[67] K. Zhong, X. Xia, B. Zhang, H. Li, Z. Wang, L. Chen, MnO powder as anode active materials for lithium ion batteries, Journal of Power Sources 195 (2010) 3300–3308.
[68] C. Chen, P.J. Perdomo, M. Fernandez, A. Barbeito, C. Wang, Porous NiO/graphene composite thin films as high performance anodes for lithium-ion batteries, Journal of Energy Storage 8 (2016) 198–204.
[69] X. Zhu, H. Shi, J. Yin, H. Zhu, Y. Zhou, Y. Tang, P. Wu, T. Lu, Facile preparation of CuO@SnO_2 nanobelts as a high-capacity and long-life anode for lithium-ion batteries, RSC Advances 4 (2014) 34417–34420.
[70] H. Wang, X. Du, X. Jiang, Y. Chai, X. Yang, R. Yuan, Pomegranate-like porous carbon coated Cu_xSn_y/Sn/SnO_2 submicrospheres as superior lithium ion battery anode, Chemical Engineering Journal 313 (2017) 535–543.
[71] D. Cao, H. Wang, B. Li, C. Li, S. Xie, A.L. Rogach, C. Niu, Hydrothermal synthesis of SnO_2 embedded MoO_{3-x} nanocomposites and their synergistic effects on lithium storage, Electrochimica Acta 216 (2016) 79–87.
[72] X. Shi, H. Song, A. Li, X. Chen, J. Zhou, Z. Ma, Sn-Co nano alloy embedded in porous N-doped carbon microboxes as a stable anode material for lithium-ion batteries, Journal of Materials Chemistry A 5 (2017) 5873–5879.
[73] W.S. Kim, Y. Hwa, H.C. Kim, J.H. Choi, H.J. Sohn, S.H. Hong, SnO_2@Co_3O_4 hollow nano-spheres for a Li-ion battery anode with extraordinary performance, Nano Research 7 (2014) 1128–1136.
[74] C. Chen, Q. Ru, S. Hu, B. An, X. Song, X. Hou, Co_2SnO_4 nanocrystals anchored on graphene sheets as high-performance electrodes for lithium-ion batteries, Electrochimica Acta 151 (2015) 203–213.
[75] Y. Cao, L. Zhang, D. Tao, D. Huo, K. Su, Facile synthesis of $CoSnO_3$/Graphene nanohybrid with superior lithium storage capability, Electrochimica Acta 132 (2014) 483–489.
[76] J. Wolfenstine, J. Allen, J. Read, D. Foster, Chemistry and structure of Sony's Nexelion Li-ion electrode materials, Army Research Lab document (2006) Online link file:///C:/Users/jdarr-xps2/Downloads/ADA479387.pdf; last accessed 22 may 2015.
[77] P. Meister, H. Jia, J. Li, R. Kloepsch, M. Winter, T. Placke, Best Practice: Performance and cost evaluation of lithium ion battery active materials with special emphasis on energy efficiency, Chemistry of Materials 28 (2016) 7203–7217.